2024 European Control Conference (ECC)
June 25-28, 2024. Stockholm, Sweden

Model-Free Control for Drop-on-Demand Droplet Generation Using Reinforcement Learning

Mikhail Vulf[1], Anton Bolychev[2], Dmitry Kolomenskiy[3] and Pavel Osinenko[4]

***Abstract*— Recently we have developed a Drop-on-Demand droplet generator which allows to generate coarse suspension droplets in a wide range of sizes (from 0.75 to 4.40 mm). However, there is a common problem that it is difficult for different liquids to generate one drop of the desired size. To solve this problem, an auto-calibration and dynamic control box is being developed. In the present work, we simulate the dynamics of a hydraulic part of the droplet generator by an experimentally verified model. This simulation is used as a black box for model-free control developed by reinforcement learning approach. The obtained results are consistent with previous droplet generation experiments. The proposed model-free control method can be used for automatic parameter adjustment for generating a single drop of different liquids.**

I. Introduction

In droplet-based 3D-printing and Coating, there are two basic methods of droplet generation: Continuous Inkjet (CIJ) and Drop-on-Demand (DoD) [1]. In this paper, we will consider the latter. There are a lot of relevant application examples of DoD droplet generator, such as Spheroid Bio-printing [2], [3], Suspension Ceramic 3D-Printing [4], Sand Molds 3D-printing [5], Metal Droplet Printing [6], etc.

In these systems, a droplet size control complexity problem becomes critical when the temperature changes, when liquids with different viscosity, surface tension and density are used, and when suspensions with high particle sedimentation speed (v_{part}) are applied (thus particle concentration $\phi(\tau)$ changes rapidly in a droplet during formation). This problem is relevant due to a large number of parameters influencing on droplet size (d_0), initial droplet velocity after detaching (v_0) and number of satellites (Fig. 1).

Recalibrations are required for nozzle clogging and the wear of moving elements, since droplet size variation and the formation of satellites lead to reduced printing quality. Also, the lack of automatic size adjustment limits the printing speed. Switching between the generation of small droplets to obtain precise geometry and the generation of large droplets to fill the printed layer would greatly speed up the printing process.

[1]Mikhail Vulf is with Center for Digital Engineering, Skolkovo Institute of Science and Technology, 121205 Moscow, Russia Mikhail.Vulf@skoltech.ru

[2]Anton Bolychev is with Center for Computational and Data Science and Engineering, Skolkovo Institute of Science and Technology, 121205 Moscow, Russia

[3]Dmitry Kolomenskiy is with Center for Materials Technologies, Skolkovo Institute of Science and Technology, 121205 Moscow, Russia

[4]Pavel Osinenko is with Center for Digital Engineering, Skolkovo Institute of Science and Technology, 121205 Moscow, Russia P.Osinenko@skoltech.ru

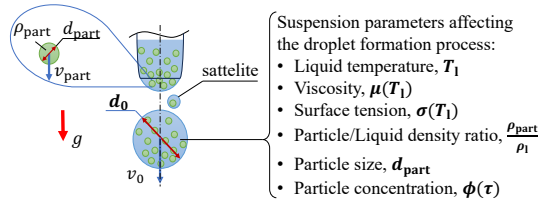

Fig. 1: Droplet formation parameters. v_{p} is a particle sedimentation speed; d_0 and v_0 are the droplet size and initial droplet velocity after detaching respectively.

To solve the problem of adjusting the size for coarse suspensions droplets, Vulf et al. [7] have developed the suspension DoD droplet generator. This droplet generator consists of the piezoelectric injector and the hydraulic machinery (Fig. 2). The latter includes a container with a hydraulic liquid and a container with a working liquid. Impulses to the working liquid are transmitted by pistons with rods.

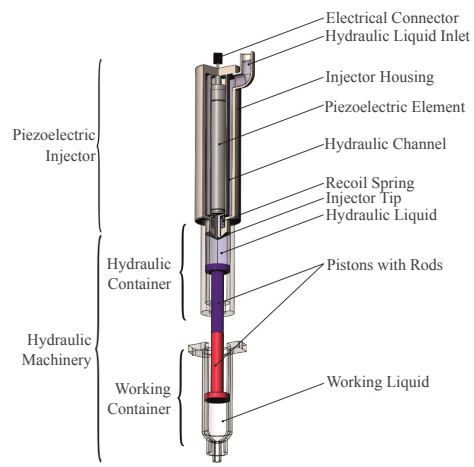

Fig. 2: Droplet generator cut-section [7].

By the container separation, this laboratory prototype allows to generate a coarse suspension and emulsion droplets (max tested particle size was 0.3 mm) in a wide range of droplet sizes (starting from 0.27 mm for pure water and from 0.75 mm for water suspensions and up to 4.40 mm), and of generation rate (from "on demand" to 1200 drops per minute) with a high droplet size repeatability (min-max range of the droplet sizes was $\pm 5.0\%$). However, it is difficult to adjust the parameters for generating a single drop of the desired size for different liquids. Manual recalibration takes a lot of

Copyright ©2024 EUCA

time.

To solve this problem, an auto-calibration and dynamic control box is developing (Fig. 3). Camera images of the generated drops are processed to determine their number and size. Based on the divergence from the desirable size, the microcontroller changes parameters of the voltage impulse $U_{\text{MCU}}(\tau)$. This impulse is amplified and supplied to the piezoelectric element $U_{\text{piezo}}(\tau)$.

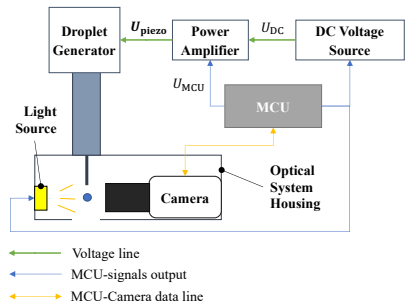

Fig. 3: Auto-calibration and dynamic control box. MCU is microcontroller unit; U_{DC} is voltage from DC Voltage Source; U_{MCU} is voltage impulse from MCU; U_{piezo} is amplified piezoelectric voltage impulse.

The injector tip postion proportional to the piezoelectric voltage ($x_{\text{th}}(\tau) \sim U_{\text{piezo}}(\tau)$). It defines the output throttle area between the injector tip and injector housing as the cylinder side surface area with injector tip diameter (D_{th}):

$$A_{\text{th}}(\tau) = \pi D_{\text{th}} x_{\text{th}}(\tau) \tag{1}$$

Through this output throttle area, hydraulic liquid flows under the pressure difference.

This paper views only the hydraulic machinery part of the controlled droplet generator (which includes the container with hydraulic liquid, the container with working liquid and pistons with rods). Hydraulic and working liquids are pure water for this research. Hydraulic machinery dynamics is quite complicated, so let us consider the model-free approach to control the hydraulic machinery.

Nowadays, the proposed model-free control for DoD droplet generator based on reinforcement learning has scientific novelty. The most relevant works are devoted to the use of reinforcement learning for droplet microfluidics control [8], [9].

II. Models

The models below describe the piston dynamics in hydraulic machinery and the droplet detaching condition when droplet detaches from the liquid jet.

A. State Dynamics Function

The calculation scheme of the hydraulic machinery system is introduced in Fig. 4. The system state parameters are the throttle position (x_{th} [μm]), piston position (x_{p} [μm]) and piston velocity (v_{p} [μm/s]):

$$x = \begin{bmatrix} x_{\text{th}} \\ x_{\text{p}} \\ v_{\text{p}} \end{bmatrix} \tag{2}$$

The injector tip position setting ($x_{\text{th}}^{\text{act}}$ [μm]) is considered as the action to the hydraulic machinery, since the injector tip position (x_{th}) cannot be changed immediately:

$$u = x_{\text{th}}^{\text{act}} \tag{3}$$

The injector tip position is a non-negative value with upper-bound $x_{\text{th}}^{\max} = 20.0$ [μm]. To model the injector tip position dynamics, constant injector tip velocity is introduced ($v_{\text{th}}^{\max} = 10^4$ [μm/s]). This velocity corresponds to the opening time of 2 ms (that is more than 1.5 ms, obtained in [10]). Jet length x_{jet} will be described in secion II-B. Micrometers are used to increase computational efficiency. Other values are in SI.

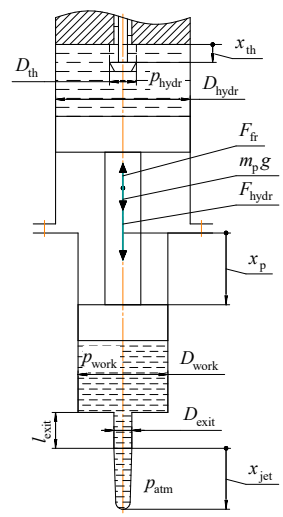

Fig. 4: Hydraulic machinery system calculation scheme. $D_\bullet$ and $p_\bullet$ denote diameter and pressure respectively; used indexes are: "th" – throttle (refers to equation (1)), "hydr" – hydraulic, "work" – working; l_{exit}, D_{exit} are orifice length and diameter respectively; x_{jet} is the current jet length (observation).

The piston moves by the action of the gravity ($m_{\text{p}}g$), hydraulic (F_{hydr}) and friction (F_{fr}) forces. Piston mass $m_{\text{p}} = 0.2 \cdot 10^{-1}$ kg (from the droplet generator prototype [7]). Let us consider hydraulic and working containers with liquid column heights 10^{-2} [m]. Then the hydrostatic pressure can be neglected. Movement starts when the acting force is larger than the friction force. The state dynamics function is thus as follows:

$$\frac{\partial x}{\partial \tau} = \begin{bmatrix} \dot{x_{\text{th}}} \\ \dot{x_{\text{p}}} \\ \dot{v_{\text{p}}} \end{bmatrix}, \qquad \dot{x_{\text{p}}} = v_{\text{p}}, \qquad \hat{x}_{\text{th}} = \text{clip}_0^{x_{\text{th}}^{\max}}(x_{\text{th}}),$$

$$\dot{x_{\text{th}}} = \begin{cases} \text{sign}(x_{\text{th}}^{\text{act}} - \hat{x}_{\text{th}}) \cdot v_{\text{th}}^{\max}, & \text{if } |x_{\text{th}}^{\text{act}} - \hat{x}_{\text{th}}| > \varepsilon_{\text{th}}^{\text{act}} \\ 0, & \text{otherwise} \end{cases}, \tag{4}$$

$$\dot{v_{\text{p}}} = \begin{cases} g + \frac{1}{m_{\text{p}}}(F_{\text{hydr}}(x_{\text{p}}, v_{\text{p}}, \hat{x}_{\text{th}}) + F_{\text{fr}}(v_{\text{p}}, F_{\text{hydr}})), \\ \qquad \text{if } |v_{\text{p}}| > 0 \text{ or } |F_{\text{hydr}} + m_{\text{p}}g| > |F_{\text{fr}}| \\ 0, \text{ otherwise} \end{cases},$$

where $\varepsilon_{\text{th}}^{\text{act}} = 0.1$ is some tip position threshold when the tip position is in satisfactory neighborhood of the setting ($x_{\text{th}}^{\text{act}}$).

Let us consider the hydraulic and friction forces separately.

1) Hydraulic force: The hydraulic force is the result of a pressure difference acting on the piston:

$$F_{\text{hydr}}(x_{\text{p}}, v_{\text{p}}, x_{\text{th}}) = A_{\text{hydr}} p_{\text{hydr}}(x_{\text{p}}, v_{\text{p}}, x_{\text{th}}) - \\ - A_{\text{work}} p_{\text{work}}(x_{\text{p}}, v_{\text{p}}), \tag{5}$$

where A_{hydr}, A_{work} are cross-sectional areas of the hydraulic and working containers respectively, determined by container diameters $(D_{\text{hydr}}, D_{\text{work}})$:

$$A_{\text{hydr}} = \frac{\pi D_{\text{hydr}}^2}{4}, \qquad A_{\text{work}} = \frac{\pi D_{\text{work}}^2}{4} \tag{6}$$

In equation (5), p_{hydr} stands for pressure in hydraulic container:

$$p_{\text{hydr}}(x_{\text{p}}, v_{\text{p}}, x_{\text{th}}) = \begin{cases} p_{\text{l}} - \frac{v_{\text{p}}|v_{\text{p}}|}{\max(c_{\text{th}}, x_{\text{th}})^2} \frac{\zeta_{\text{th}} \rho_{\text{hydr}} D_{\text{hydr}}^4}{32 D_{\text{th}}^2}, \\ \quad \text{if } x_{\text{th}} > 0 \\ p_{\text{hydr}}\big|_{x_{\text{th}}>0} + \\ \quad + \left(\frac{x_{\text{p}}\big|_{x_{\text{th}}>0}}{x_{\text{p}}} - 1 \right) \frac{1}{\beta_{V_{\text{hydr}}}}, \\ \quad \text{otherwise} \end{cases}, \tag{7}$$

where $p_{\text{l}} = 0.25 \cdot 10^6$ [Pa] is absolute hydraulic liquid pressure before throttling (used in experiments [7]); $\zeta_{\text{th}} = 5.0$ is local hydraulic resistance coefficient (taken as for a valve and can be determined experimentally); $\rho_{\text{hydr}} = 10^3$ [kg/m^3] (for water) is hydraulic liquid density; $\beta_{V_{\text{hydr}}} = -\frac{1}{V}\frac{\partial V}{\partial p} = \text{const} = 0.49 \cdot 10^{-9}$ [Pa^{-1}] (for water) is coefficient of hydraulic liquid compressibility; $p_{\text{hydr}}\big|_{x_{\text{th}}>0}$, $x_{\text{p}}\big|_{x_{\text{th}}>0}$ are last hydraulic pressure and piston position when the throttle was opened; term $v_{\text{p}}|v_{\text{p}}|$ allows to consider the sign of the flow through the throttle; $D_{\text{hydr}} = 0.2 \cdot 10^{-1}$ [m]; $D_{\text{th}} = 0.2 \cdot 10^{-3}$ [m]; $c_{\text{th}} = 0.5$ is some backlash of the injector tip position. If throttle is opened, tip position is not less than c_{th}. This trick allows to prevent dividing on a small value, when x_{th} is closed to zero.

Equation (7) was derived based on the Darcy–Weisbach equation and equation (1) for the open throttle $(x_{\text{th}} > 0)$ and on the isothermal compressibility of the hydraulic liquid for the closed throttle $(x_{\text{th}} = 0)$.

In equation (5), p_{work} is the pressure in the working container:

$$\begin{aligned} p_{\text{work}}(x_{\text{p}}, v_{\text{p}}) &= p_{\text{atm}} + p_{\text{cap}}(x_{\text{p}}) + v_{\text{p}}|v_{\text{p}}| \frac{\zeta_{\text{exit}} \rho_{\text{work}} D_{\text{work}}^4}{2 D_{\text{exit}}^4 \cdot 10^{12}}, \\ p_{\text{cap}}(x_{\text{p}}) &= \text{sign}(x_{\text{p}} - x_{\text{p0}}) \cdot \min\left(\frac{4\sigma_{\text{work}}}{D_{\text{exit}}}, p_{\text{compr}}(x_{\text{p}}) \right), \\ p_{\text{compr}}(x_{\text{p}}) &= \left| \frac{x_{\text{p}} - x_{\text{p0}}}{x_{\text{p}}} \right| \frac{1}{\beta_{V_{\text{work}}}}, \end{aligned} \tag{8}$$

where $p_{\text{atm}} = 0.1 \cdot 10^6$ [Pa] is atmosphere pressure; $x_{\text{p0}} = 10^3$ [μm] is initial pistion position; p_{cap} is capillary pressure in assumption that liquid-air surface is flat (curvature equals to zero) when $x_{\text{p}} = x_{\text{p0}}$ (thus $p_{\text{cap}} = 0$), and capillary pressure modular increases by liquid compressibility $(p_{\text{compr}}(x_{\text{p}}))$ until it reaches value $\left(\frac{4\sigma_{\text{work}}}{D_{\text{exit}}}\right)$ when jet extracts from the orifice (experimentally validated in [11]); $\rho_{\text{work}} = 10^3$ [kg/m^3], $\sigma_{\text{work}} = 0.73 \cdot 10^{-1}$ [N/m] (for water) are working liquid density and surface tension respectively; $\beta_{V_{\text{work}}} = 0.49 \cdot 10^{-9}$ [Pa^{-1}] (for water) is coefficient of working liquid compressibility; $\zeta_{\text{exit}} = \frac{1}{C_{\text{D}}^2}$, $C_{\text{D}} = 0.827 - 0.0085 \frac{l_{\text{exit}}}{D_{\text{exit}}}$ is discharge coefficient [12, P. 8-9]; $l_{\text{exit}} = 0.85 \cdot 10^{-2}$ [m], $D_{\text{exit}} = 0.33 \cdot 10^{-3}$ [m] are text container orifice length and diameter respectively; $D_{\text{work}} = 0.2 \cdot 10^{-1}$ [m]; coefficient 10^{12} appears since v_{p} is in μm/s. All sizes are taken from the droplet generator prototype [7].

2) Friction force: Friction force is estimated by the mechanical efficiency approach. When the piston does not move, it must overcome the Coulomb friction force (F_{C}) to start moving. When piston moves, friction force is the maximum between Coulomb friction force and hydraulic force losses determined by the mechanical efficiency $\eta = 0.7$:

$$F_{\text{fr}}(v_{\text{p}}, F_{\text{hydr}}) = \begin{cases} -\text{sign}(v_{\text{p}}) \cdot \max(F_{\text{C}}, (1-\eta) F_{\text{hydr}}), \\ \quad \text{if } |v_{\text{p}}| > 0 \\ -\text{sign}(F_{\text{hydr}} + m_{\text{p}} g) \cdot F_{\text{C}}, \\ \quad \text{otherwise} \end{cases} \tag{9}$$

where $F_{\text{C}} = p_{\text{C}} \max(A_{\text{hydr}}, A_{\text{work}})$, $p_{\text{C}} = 10^4$[Pa] is pressure difference, which is necessary to overcome the dry friction.

B. Droplet Detaching Condition

According to linear stability analysis and experiments conducted by Grant and Middleman [13], there is a critical (breakup) jet length ($x_{\text{jet}} = l_{\text{crit}}$ [mm], Fig. 4), after which the drop separates. This critical jet length may be defined by Reynolds number (Re) and Weber number (We):

$$\begin{aligned} \frac{l_{\text{crit}}}{D_{\text{exit}}} &= 19.5 \cdot 10^3 \ \text{We}^{0.5} (1 + 3\text{Oh})^{0.85}, \\ \text{We} &= \frac{\rho_{\text{work}} v_{\text{j}}^2 D_{\text{exit}}}{10^6 \sigma_{\text{work}}}, \quad \text{Oh} = \frac{\sqrt{\text{We}}}{\text{Re}}, \\ \text{Re} &= \frac{\rho_{\text{work}} v_{\text{j}} D_{\text{exit}}}{10^3 \mu_{\text{work}}}, \end{aligned} \tag{10}$$

where $\mu_{\text{work}} = 10^{-3}$ [Pa · s] (for water) is the dynamic viscosity of the working liquid; $v_{\text{j}} = 0.2 \cdot 10^3$ [mm/s] is jet velocity (empirically estimated in [7]); coefficients 10^6 and 10^3 appear since jet velocity is in mm/s. Other values are in SI.

Research of pneumatic DoD generator, conducted by Cheng and Changra [11], showed that jet critical length estimation (10) may be used also as the single droplet detaching criterion: droplet detaches from jet if $x_{\text{jet}} \geq l_{\text{crit}}$. However, Cheng and Changra [11] noticed that the longer the jet length, the more satellites are formed. Thus, our control goal is as follows:

$$x_{\text{jet}} \searrow l_{\text{crit}} \tag{11}$$

This means that the jet length should be above the critical jet length, but converge to it.

The size of the detached droplet D_{d} [mm] can be estimated by [11]:

$$\frac{D_{\text{d}}}{D_{\text{exit}}} = 10^3 (1.5\pi\sqrt{2 + 3\text{Oh}})^{1/3} \tag{12}$$

Thus, for the sizes of the droplet generator prototype described previously, $l_{\text{crit}} = 1.92$ [mm] and $D_{\text{d}} = 0.622$ [mm]. Droplet diameter is in the range obtained experimentally in the droplet generator prototype research [7].

C. Observations

Let us assume, that camera in Fig. 3 allows to retrieve current jet length (x_{jet} [mm]) and calculate jet velocity (v_{jet} [mm/ms]) as system observations with noise:

$$\begin{aligned} &y = \begin{bmatrix} x_{\text{jet}} \\ v_{\text{jet}} \end{bmatrix}, \qquad \varepsilon_x \sim \mathcal{N}(0, \sigma_x^2), \qquad \varepsilon_v \sim \mathcal{N}(0, \sigma_v^2), \\ &\hat{x}_{\text{jet}} = 10^{-3} \frac{D_{\text{work}}^2}{D_{\text{exit}}^2}(x_{\text{p}} - x_{\text{p0}}), \qquad \hat{v}_{\text{jet}} = 10^{-6} \frac{D_{\text{work}}^2}{D_{\text{exit}}^2} v_{\text{p}}, \\ &x_{\text{jet}} = \hat{x}_{\text{jet}} + l_{\text{crit}} \varepsilon_x, \qquad v_{\text{jet}} = \hat{v}_{\text{jet}} + 10^{-3} \frac{l_{\text{crit}}}{\Delta\tau} \varepsilon_v, \end{aligned} \tag{13}$$

where ε_x, ε_v are random noise values sampled from normal distributions with standard deviations $\sigma_x = 0.05$, $\sigma_v = 0.01$ respectively; $\hat{x}_{\text{jet}}$, $\hat{v}_{\text{jet}}$ are real jet length and jet velocity without noise, 10^{-3} and 10^{-6} here are used to convert [μm] to [mm] and [μm/s] to [mm/ms] respectively. We convert them for computational efficiency. $\Delta\tau$ is a control time step duration, which is described in section IV.

The models from this section are used only for the environment simulation. The reinforcement learning algorithm have no access to the system state. Only observations are used for the learning procedure as control input.

III. Reinforcement Learning Procedure

Let us proceed to the Model-free control approach implemented in this paper. REINFORCE Algorithm with baseline [14] was used to train weights θ of the stochastic control policy model $\rho^\theta(u \mid y)$.

A. Policy Model

The policy model treats as a normal probability distribution, so actions are sampled from this distribution:

$$u \sim \rho^\theta(u \mid y) = \mathsf{pdf}_{\mathcal{N}(\lambda\mu_\theta(y)+\beta, \lambda^2\sigma^2)}(u), \tag{14}$$

where $\mathsf{pdf}_{\mathcal{N}(\bullet_1, \bullet_2)}$ refers to the normal probability density function with mean $\bullet_1$ and (co)variance $\bullet_2$; $\beta = \frac{U_{\min}+U_{\max}}{2}$, $\lambda = \frac{U_{\max}-U_{\min}}{2}$; $U_{\min}$, $U_{\max}$ are the minimum and maximum action respectively. In our simulations we put $\sigma = 0.01$.

Let us choose $U_{\min}$, $U_{\max}$ in such a way, that:

$$\begin{aligned} &U_{\min} < (x_{\text{th}}^{\min} = 0), \\ &U_{\max} > (x_{\text{th}}^{\max} = 20.0 \text{ [μm]}) \end{aligned} \tag{15}$$

This approach allows to consider negative actions as a total closure of the throttle and actions larger than $x_{\text{th}}^{\max}$ as full throttle opening. It is important, since the policy model must learn to close the throttle after reaching the critical jet length. In this paper the following limits are used: $U_{\min} = -20$ [μm]; $U_{\max} = 30$ [μm]. System limits action to possible injector tip position range [0, 20.0] μm (see $\hat{x}_{\text{th}}$ in equation (4)).

In equation (14), $\mu_\theta(\bullet)$ is a perceptron with weights θ:

$$\begin{aligned} &\mu_\theta(y) : y \to \text{Linear}(2,\ 2) \to \text{LeakyReLU}(0.2) \to \\ &\to \text{Linear}(2,\ 2) \to \text{LeakyReLU}(0.2) \to \\ &\to \text{Linear}(2,\ 1) \to (1 - 3\sigma)\tanh\left(\frac{\bullet}{L}\right) \end{aligned} \tag{16}$$

where hyperparameter L is merely a tuning parameter and does not posess a physical meaning. In our simulations we put $L = 10$.

The last activation layer in the equation (16) limits the perceptron output: $\mu_\theta(y) \in [-1 + 3\sigma,\ 1 - 3\sigma]$. Since the operation $(\lambda \cdot [\bullet] + \beta)$ transforms $[-1,\ 1]$ to $[U_{\min},\ U_{\max}]$, the policy model $\rho^\theta(u \mid y)$ samples actions that are within action bounds $[U_{\min},\ U_{\max}]$ with propability greater than 99.7% by 3σ-rule. If actions are sampled out of this bounds, we clip them to $[U_{\min},\ U_{\max}]$.

B. Running Cost Function

This policy model $\rho^\theta(u \mid y)$ is trained to achieve the control goal (11) while optimizing some running cost $c(y, u)$:

$$\begin{aligned} &c(x_{\text{jet}}) = \left(1 - x_{\text{jet}}^{\text{rel}}\right)^2, \\ &x_{\text{jet}}^{\text{rel}} = \frac{x_{\text{jet}}}{l_{\text{crit}}}, \qquad v_{\text{jet}}^{\text{rel}} = \frac{v_{\text{jet}}}{l_{\text{crit}}}, \end{aligned} \tag{17}$$

where $x_{\text{jet}}^{\text{rel}}$ is a relative jet length (we want to obtain $x_{\text{jet}}^{\text{rel}} = 1.0$) and $v_{\text{jet}}^{\text{rel}}$ [1/ms] is a relative jet velocity. Thus, the running cost (17) penalizes the policy $\rho^\theta(u \mid y)$ for the relative difference between current jet length (x_{jet}) and critical (breakup) jet length (l_{crit}) which is necessary to achieve. We do not penalize the model for the relative jet velocity $v_{\text{jet}}^{\text{rel}}$ and the action u.

C. REINFORCE step

The general formula of the REINFORCE gradient step is as follows:

$$\theta_{i+1} \leftarrow \theta_i - \alpha\mathbb{E}\left[\sum_{t=1}^{T} (C_t - B_t)\, \nabla_\theta \ln \rho^\theta(U_t \mid Y_t)\big|_{\theta=\theta^i}\right], \tag{18}$$

where $C_t = \sum_{t'=t}^{T} \gamma^{t'} c(Y_{t'}, U_{t'})$ are the costs-to-go; B_t is the baseline – a random variable independent on (Y_t, U_t); γ is a discount factor; α is a learning rate; t is a control time step; i is an iteration step index. In our simulations, we put $\gamma = 1$, $\alpha = 0.05$. In the equation (18), we use capital letters (C_t, B_t, U_t, Y_t) to emphasize that these variables are random.

Full REINFORCE Algorithm with baseline is listed below (see Algorithm 1).

where I is the number of iterations; M is the number of episodes; T is the number of steps inside an episode. In our simulations we put $T = 10$, $M = 5$, $I = 200$. Baselines are computed as previous means of tail objectives.

IV. Simulation and Discussion

We programmed the REINFORCE with baseline (Algorithm 1) using the Python programming language (3.9.6). One control time step (t, see equation (18)) is a time step with duration $\Delta\tau = 10^{-3}$ s. The 1 kHz control update rate is

Algorithm 1: REINFORCE with baseline

Initialize baseline for the 1st iteration: $b^1 \leftarrow 0$;
for $i = 1, 2, ..., I$ **do**
  `// i is iteration index`
  for $j = 1, 2, ..., M$ **do**
    `// j is episode index`
    for $t = 1, 2, ..., T$ **do**
      `// t is time step index`
      obtain observation y_t^j from system;
      sample action u_t^j from $\rho^\theta\left(u_t^j | y_t^j\right)$;
    end
  end

  For all $t = 1, 2, ...T$ compute baselines for the next iteration:

$$b_t^{i+1} \leftarrow \frac{1}{M}\sum_{j=1}^{M}\sum_{t'=t}^{T}\gamma^{t'}c\left(y_{t'}^j, u_{t'}^j\right);$$

  Let us denote costs-to-go as:

$$C_t^j \leftarrow \sum_{t'=t}^{T}\gamma^{t'}c\left(y_{t'}^j, u_{t'}^j\right);$$

  Perform a gradient step:

$$\theta_{i+1} \leftarrow \theta_i - \frac{\alpha}{M}\sum_{j=1}^{M}\sum_{t=1}^{T}\left(C_t^j - b_t^i\right)\nabla_\theta \ln\rho^\theta(u_t^j \mid y_t^j)\big|_{\theta=\theta^i};$$

end

achieved using a line scan camera and a high-speed computer vision algorithm to get jet observations [15], [16]. The piezoelectric injector can also act at an operating frequency of 1 kHz [10], [17].

Thus, at $T = 10$ the entire duration of the episode is $\tau_{\text{episode}} = 10$ ms. During one control step with period $\Delta\tau$, the constant action $(x_{\text{th}}^{\text{act}})$ sampled from the policy model (14) is applied to the hydraulic system. The hydraulic system dynamics (4) are modeled during this one control time step $\Delta\tau$ by the adaptive Runge-Kutta method "RK45". The initial conditions (with $\tau_0 = 0$) are:

$$x_{\text{th}0} = 0, \quad x_{\text{p}0} = 10^3 \text{ [µm]}, \quad v_{\text{p}0} = 0 \tag{19}$$

The initial pressures in the containers are: $p_{\text{hydr}0} = p_{\text{work}0} = p_{\text{atm}}$. The equality $(p_{\text{work}0} = p_{\text{atm}})$ is achieved by equation (8). To obtain the equality $(p_{\text{hydr}0} = p_{\text{atm}})$ for the hydraulic container, we set as initial conditions (only for $\tau = 0$): $p_{\text{hydr}}\big|_{x_{\text{th}}>0,\tau=0} = p_{\text{atm}}$ and $x_{\text{p}}\big|_{x_{\text{th}}>0,\tau=0} = x_{\text{p}0}$.

The simulation is carried out on a workstation that has 6 cores with 3.6 GHz CPU, 32 Gb RAM. The quality of the policy model at each iteration is evaluated with the help of the total cost (average by episodes), evaluated by real jet length $\hat{x}_{\text{jet}}(t)$ at the moment t (without noise):

$$C_{\text{total}} = \frac{1}{M}\sum_{j=1}^{M}\sum_{t=1}^{T}\gamma^t c\left(\hat{x}_{\text{jet}}(t)\right) \tag{20}$$

A learning process for five seeds is introduced in Fig. 5. This plot shows the change in the total cost from iteration to iteration (Our controller). P-controller with $P = U_{\max}$ is used as a Benchmark.

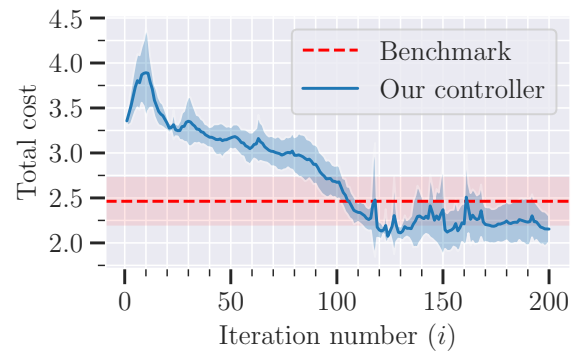

Fig. 5: Learning curve: total cost (20) by iteration (average by five seeds). Regions around the charts correspond to the standard deviations $\pm\sigma$ obtained on simulated seeds.

At the beginning of the learning process, the policy model samples positive actions according to the initial random weights (θ^0). Then the total cost begins to decrease, since the policy model samples greater actions at the beginning and smaller actions at the end of the episode. The former allows to reach the critical jet length l_{crit} as fast as possible, and the latter reduces the rate of jet length growth (or jet velocity v_{jet}) after reaching the critical jet length. Thus, the relative jet length $(x_{\text{jet}}^{\text{rel}})$ is getting closer to one from iteration to iteration.

Finally, the total cost (averaged by seeds) reduces during first 125 iterations and becomes the lowest due to setting the maximum action at the beginning and the negative action at the moment $\tau = 2$ ms to stop the relative jet length growth (Fig. 6). Let us remind that actions $x_{\text{th}}^{\text{act}} > 20$ µm are considered as total opened throttle ($x_{\text{th}} = 20$ µm) and actions $x_{\text{th}}^{\text{act}} < 0$ µm – as total closed throttle ($x_{\text{th}} = 0$ µm) (see black horizontal lines on the action plot, Fig. 6; equations (4) and (15)).

Let us discuss the obtained result and consider actions $(u = x_{\text{th}}^{\text{act}})$ sampled from the policy model $(\rho^\theta(u \mid y)|_{\theta=\theta^i})$ on the last iteration $(i = 200)$. In Fig. 6, these actions are introduced with the relative observations: the relative jet velocity $(v_{\text{jet}}^{\text{rel}})$ and relative jet length $(x_{\text{jet}}^{\text{rel}})$ (see equation (17)) depending on time (τ). Due to the limited injector tip velocity $v_{\text{th}}^{\max}$, the jet stops growth only after $\tau = 4$ ms, when the drop detaching condition achieved $(x_{\text{jet}}^{\text{rel}} > 1.0)$. The jet with relative length $x_{\text{jet}}^{\text{rel}} = 1.14$ was obtained (versus 1.39 for the Benchmark). The averaged by seeds total cost was decreased to 2.07 for our controller, while the Benchmark average total cost is 2.46. Thus, the average total cost was reduced by more than 15%.

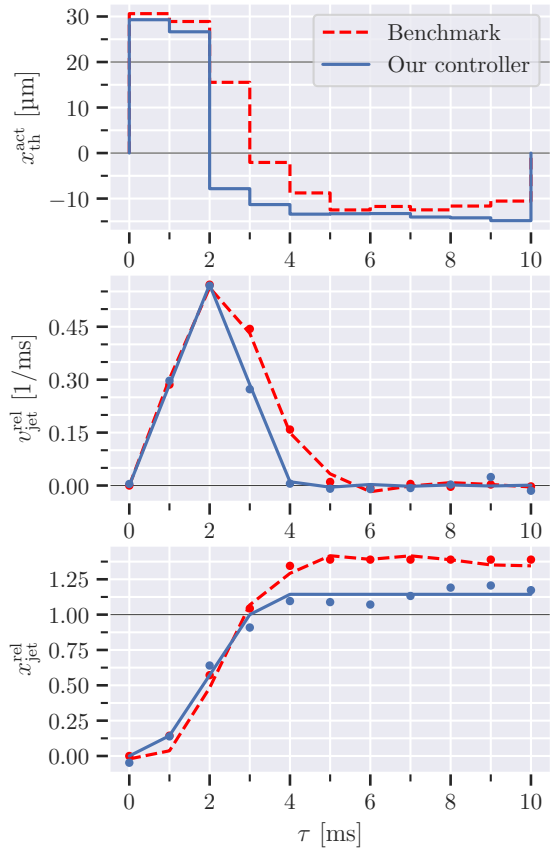

Fig. 6: Simulation results at the last iteration ($i = 200$). The results correspond to an arbitrary selected seed. τ is the time in the simulation. Upper and lower black horizontal lines on the action plot (first plot) determine the complete opening and complete closing of the throttle respectively. Black horizontal lines on the plots of the relative jet velocity and the relative jet length (last two plots) show the control goal which is necessary to achieve.

The optimized policy model keeps the throttle fully open for $\Delta\tau = 2$ ms and total closes it at $\tau = 2$ ms (action plot, Fig. 6).

V. Conclusions

Thus, the optimized policy learned by a model-free approach (REINFORCE with baseline) reduced the average total cost of the Benchmark by more than 15%. This policy can be interpreted as a single pulse with $\Delta\tau = 2$ ms duration and $x_{th}^{act} = 20$ µm amplitude. The droplet generation experiments with single pulse mode were conducted in our previous work [7]. A high speed camera (Photron Mini UX100, Tokyo, Japan) was used to record droplet formation process. The pulses were generated by a microcontroller unit (Arduino UNO R3, Italy). The pulse parameters ($\Delta\tau = 4$ ms duration and $x_{th}^{act} = 10 \pm 1$ µm amplitude) were obtained manually by observations processing after each calibration test. Results were collected in the parametric map. The experimental impulse was simulated by the hydraulic machinery dynamics model (4) and a jet with relative length $x_{jet}^{rel} = 1.15$ was obtained – a droplet was generated. Thus, the hydraulic machinery dynamics model was verified.

The optimized policy actions qualitatively coincides with pulses applied experimentally to generate a single droplet of water and quantitatively close to it. The area under the simulated impulse is very close to the experimental impulse area. However, the experiments [7] used predefined impulse parameters and did not apply actions depending on the observation in real-time mode. To automate the parameter selection process, the auto-calibration and dynamic control box is being developed. The suggested model-free control method will be tested with the auto-calibration and dynamic control box, mounted on the experimental facility [7]. The proposed setup will automatically adjust the droplet generator parameters to produce a single drop of various liquids.

References

[1] J. R. Castrejón-Pita, S. J. Willis, and A. A. Castrejón-Pita, "Dynamic nozzles for drop generators," *Review of Scientific Instruments*, vol. 86, no. 11, nov 2015.

[2] H. Gudapati, M. Dey, and I. Ozbolat, "A comprehensive review on droplet-based bioprinting: Past, present and future," *Biomaterials*, vol. 102, pp. 20–42, sep 2016.

[3] A. Persaud, A. Maus, L. Strait, and D. Zhu, "3d bioprinting with live cells," *Engineered Regeneration*, vol. 3, no. 3, pp. 292–309, sep 2022.

[4] U. Scheithauer, "Droplet-based additive manufacturing of hard metal components by thermoplastic 3d printing (t3dp)," 2017.

[5] M. Upadhyay, T. Sivarupan, and M. E. Mansori, "3d printing for rapid sand casting—a review," *Journal of Manufacturing Processes*, vol. 29, pp. 211–220, oct 2017.

[6] J. Szczech, C. Megaridis, D. Gamota, and J. Zhang, "Fine-line conductor manufacturing using drop-on demand PZT printing technology," *IEEE Transactions on Electronics Packaging Manufacturing*, vol. 25, no. 1, pp. 26–33, jan 2002.

[7] M. Vulf, V. Petrov, A. Sulimov, A. Simonova, A. Kazak, S. Chugunov, and D. Kolomenskiy, "A novel droplet generator and a bench-testing rig enabling research on suspension droplet wall impingement and particle deposition," *Coatings*, vol. 13, no. 1, p. 129, jan 2023.

[8] N. Gyimah, O. Scheler, T. Rang, and T. Pardy, "Deep reinforcement learning-based digital twin for droplet microfluidics control," *Physics of Fluids*, vol. 35, no. 8, aug 2023.

[9] O. J. Dressler, P. D. Howes, J. Choo, and A. J. deMello, "Reinforcement learning for dynamic microfluidic control," *ACS Omega*, vol. 3, no. 8, pp. 10 084–10 091, aug 2018.

[10] D. Branson, F. Wang, D. Johnston, D. Tilley, C. Bowen, and P. Keogh, "Piezoelectrically actuated hydraulic valve design for high bandwidth and flow performance," *Proceedings of the Institution of Mechanical Engineers, Part I: Journal of Systems and Control Engineering*, vol. 225, no. 3, pp. 345–359, 5 2011.

[11] S. Cheng and S. Chandra, "A pneumatic droplet-on-demand generator," *Experiments in Fluids*, vol. 34, no. 6, pp. 755–762, 6 2003.

[12] C. T. Crowe and C. T. Crowe, Eds., *Multiphase Flow Handbook*. CRC Press, sep 2005.

[13] R. P. Grant and S. Middleman, "Newtonian jet stability," *AIChE Journal*, vol. 12, no. 4, pp. 669–678, jul 1966.

[14] R. S. Sutton and A. G. Barto, *Reinforcement Learning: An Introduction*. Cambridge, MA, USA: A Bradford Book, 2018.

[15] D. Jasper and S. Fatikow, "Line scan-based high-speed position tracking inside the sem," *International Journal of Optomechatronics*, vol. 4, no. 2, pp. 115–135, 5 2010.

[16] S. Van Wolputte, W. Abbeloos, S. Helsen, A. Bey-Temsamani, and T. Goedeme, *Embedded line scan image sensors: The low cost alternative for high speed imaging*. IEEE, 11 2015.

[17] D. Roberts, H. Li, J. Steyn, O. Yaglioglu, S. Spearing, M. Schmidt, and N. Hagood, "A piezoelectric microvalve for compact high-frequency, high-differential pressure hydraulic micropumping systems," *Journal of Microelectromechanical Systems*, vol. 12, no. 1, pp. 81–92, 2 2003.